Estimation of Enceladus Plume Density Using Cassini Flight Data

Eric K. Wang* and Allan Y. Lee†
Jet Propulsion Laboratory, California Institute of Technology, Pasadena, California

Abstract

The Cassini spacecraft was launched on October 15, 1997 by a Titan 4B launch vehicle. After an interplanetary cruise of almost seven years, it arrived at Saturn on June 30, 2004. In 2005, Cassini completed three flybys of Enceladus, a small, icy satellite of Saturn. Observations made during these flybys confirmed the existence of water vapor plumes in the south polar region of Enceladus. Five additional low-altitude flybys of Enceladus were successfully executed in 2008-9 to better characterize these watery plumes. During some of these Enceladus flybys, the spacecraft attitude was controlled by a set of three reaction wheels. When the disturbance torque imparted on the spacecraft was predicted to exceed the control authority of the reaction wheels, thrusters were used to control the spacecraft attitude. Using telemetry data of reaction wheel rates or thruster on-times collected from four low-altitude Enceladus flybys (in 2008–10), one can reconstruct the time histories of the Enceladus plume jet density. The 1σ uncertainty of the estimated density is 5.9–6.7% (depending on the density estimation methodology employed). These plume density estimates could be used to confirm measurements made by other onboard science instruments and to support the modeling of Enceladus plume jets.

*Member of Technical Staff, Guidance and Control Flight Software Validation Section, 4800 Oak Grove Dr., M.S. 230-104, Pasadena, CA 91109-8099. AIAA member. Lead Flight Software Engineer, Attitude and Articulation Control Subsystem, Cassini Spacecraft Operations Office.
†Section Staff, Guidance and Control Section. AIAA member. Team Lead, Attitude and Articulation Control Subsystem, Cassini Spacecraft Operations Office, 1999–2009.

Acronyms

AACS	Attitude and Articulation Control System	RCS	Reaction Control System (Thrusters)
BOB	Bang-Off-Bang	RHS	Right Hand Side (of an equation)
ECA	Enceladus Closest Approach	RSS	Root Sum of Squares
JPL	Jet Propulsion Laboratory	RWA	Reaction Wheel Assembly
LHS	Left Hand Side (of an equation)	S/C	Spacecraft
mrad	milliradian (1° = 17.4533 mrads)	SCET	Spacecraft Event Time

I. Cassini/Huygens Mission to Saturn and Titan

As the first spacecraft to achieve orbit at Saturn in 2004, Cassini has collected science data throughout its four-year prime mission and has since been approved for a first and second extended mission through 2017. Major science objectives of the Cassini mission include investigations of the configuration and dynamics of Saturn's magnetosphere, the structure and composition of the rings, the characterization of several of Saturn's icy satellites, and Titan's atmosphere constituent abundance. The radar mapper will perform surface imaging and altimetry during many Titan flybys. Doppler tracking experiments using the Earth and the Cassini spacecraft as separated test masses have also been conducted for gravitational wave searches.

After an interplanetary cruise that lasted almost seven years, on June 30, 2004, Cassini fired one of its two rocket engines for about 96 minutes in order to slow the spacecraft's velocity (by about 626.17 m/s) to allow the spacecraft to be captured by the gravity field of Saturn. This was the most critical engineering event of the entire mission and was executed faultlessly. After the completion of the Saturn Orbit Insertion, Cassini began a complicated suite of orbits about Saturn, designed to optimize science collection over not only Saturn, but also its moons. The orbital tour of Saturn includes over fifty flybys of Saturn's largest moon, Titan. At 5150 kilometers in diameter, Titan is larger than the planet Mercury. While one of the Cassini-Huygens Mission primary objectives was the study of Titan via many close flybys during its four-year tour, the exciting discovery of water geysers emanating from Enceladus drove an extensive redesign of the extended mission orbital tour of Saturn.

II. The Discovery of Watery Geysers From Enceladus

Enceladus is a small, icy satellite of Saturn with a mean radius of 252.3 km. Covered in water ice that reflects sunlight like freshly fallen snow, Enceladus reflects almost 100% of the sunlight that strikes it making it one of the brightest objects in the solar system. Due to the fact that Enceladus reflects so much sunlight, the surface temperature is extremely cold, about -201°C. Parts of Enceladus show craters no larger than 35 km in diameter while other areas show regions with no craters indicating major resurfacing events in the geologically recent past. There are fissures, plains, corrugated terrain, and other crustal deformations. All of this indicates that the interior of the moon may be liquid today even though it should have been frozen eons ago.

In 2005, Cassini made three flybys of Enceladus: a 1264-km Enceladus-0 flyby on February 17, 2005, a 500-km Enceladus-1 flyby on March 9, 2005, and a 175-km Enceladus-2 flyby on July 14, 2005. Observations made during these flybys confirmed the existence of a water vapor plume in the south polar region of Enceladus.[1-5] Cassini's Ion and Neutral Mass Spectrometer made measurements of the plume density out to a distance of 4,000 km from the surface of Enceladus. The radial and angular distributions of the INMS-based density estimates suggest a significant contribution to the plume from a source centered near the south polar cap of Enceladus.[2]

Cassini imaging science instruments[1,3] revealed four prominent linear fractures, each separated by about 30 km and spanning 130 km in length, straddling the South polar region. These fractures, informally termed "Tiger stripes," show dark flanks in the near-IR and are anomalously warm. They are identified individually as Alexandria, Cairo, Baghdad, and Damascus. The Tiger stripes are a likely source of tectonic activities and plume generation. From these Tiger stripes, materials are vented from the interior of the moon to hundreds of kilometers above the moon's surface. One estimate of the "height" of these plumes is 300 km from the surface.[2] Reference 5 conjectured that the Enceladus plume might be the dominant source of materials in the Saturn's E ring system.

The discovery of watery geysers from Enceladus is an important and unexpected discovery made by Cassini. The Enceladus watery plume was one of the key science investigations of the Cassini Equinox mission (an extension of the Cassini Prime mission, from July 2008 to September 2010). It still remains as one of the key science objectives for the Cassini Solstice Mission (a second mission extension, from October 2010 to May 2017). Eleven Enceladus flybys are currently planned for the Cassini Solstice Mission. Using attitude control telemetry data, plume

jet densities encountered during four low-altitude Enceladus flybys are reconstructed in this work. These are flybys that passed through the plume jets with closest approach altitudes that are less than or equal to 100 km. Details of the selected Enceladus flybys are given in Table 1.

Table 1. Descriptive Statistics of Targeted Low-altitude Enceladus Flybys Studied

Flyby Designation	Date of Flyby And ECA Time	Distance at Closest Approach [km]	Location of Closest Approach (β_{LAT}, β_{LON})	Enceladus-relative flyby velocity [km/s]	Spacecraft Control Mode
Enceladus-3	03/12/2008T19:06:12	47.9	20° S, 135° W	14.412	RWA
Enceladus-5	10/09/2008T19:06:40	28.98	28° S, 97° W	17.733	RCS (A-branch)
Enceladus-7	11/02/2009T07:41:58	102.69	82° S, 159° W	7.741	RCS (B-branch)
Enceladus-9	04/28/2010T00:10:17	102.7	89° S, 147° W	6.515	RWA

III. Cassini Spacecraft Reaction Wheel and Thruster Control System Designs[6,9,10]

Cassini is perhaps the largest and most sophisticated interplanetary spacecraft humans have ever built and launched. The orbiter is about 6.8 m in height with a "diameter" of 4 meters. The total mass of the spacecraft at launch was approximately 5,574 kg, which includes about 3,000 kg of bi-propellant (1,869 kg of Nitrogen Tetroxide, and 1,131 kg of mono-methyl hydrazine), 132 kg of high purity hydrazine, and 2,442 kg of "dry" mass (including the 320-kg Huygens Probe and 9 kg of helium mass).

Cassini carries a set of three "strap-down" reaction wheels that are mounted on the lower equipment module. They are oriented "equal distance" from the spacecraft's Z-axis. The first use of the reaction wheel control was on March 16, 2000, several months ahead of the Jupiter science campaign that began on October 1, 2000. A backup reaction wheel assembly (RWA) is mounted on top of an articulatable platform. At launch, the backup reaction wheel is mounted parallel to reaction wheel assembly #1 (RWA-1). On July 11, 2003, the platform was articulated in order to align the backup reaction wheel with RWA-3. Figure 1 (from Ref. 10) is an illustration of the RWA controller (RWAC) design.

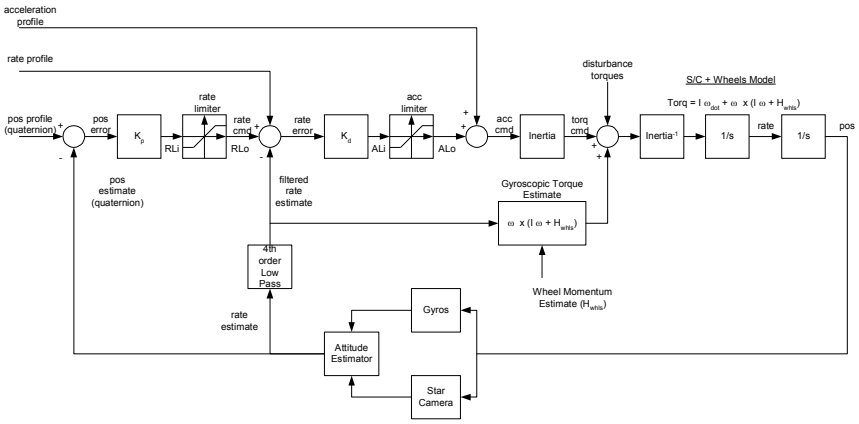

Fig. 1. Block Diagram of the Reaction Wheel-based Attitude Control System[10]

Since Cassini spacecraft's principle axes are very closely aligned with the spacecraft's mechanical axes, the basic structure of the RWAC is a decoupled, three-axis, Proportional and Derivative controller. As indicated in Fig. 1, the control torque is determined using the equation:

$$\text{Control Torque} = I_{SC}\frac{d\omega}{dt} + \omega \times (I_{SC}\omega + H_{RWA}) \tag{1}$$

Here, ω is the spacecraft angular rate vector (that is expressed in a body-fixed coordinate frame), H_{RWA} represents the total angular momentum vector of the three prime wheels (that is also expressed in the body frame), I_{SC} is the inertia tensor of the vehicle, and $d\omega/dt$ is the spacecraft's angular acceleration. The second term in Eq. (1) represents the gyroscopic torque vector.

Due to the presence of bearing frictional torque in the reaction wheels, an RWAC with the "PD" (Proportional + Derivative) control architecture will not be able to drive the spacecraft attitude control error to zero unless an integral term is added to the PD controller. This difficulty was overcome by the addition of a Proportional and Integral estimator of the reaction wheel frictional torque in the reaction wheel "hardware manager." In effect, integral control action is added "locally" to remove any steady-state spacecraft attitude control errors. Further design details are described in Ref. 10. The RWAC design has a bandwidth of 0.0299 Hz. Flight performance of the RWAC is described in References 8–10.

During early Cruise, Cassini used a set of eight thrusters to maintain three-axis attitude control of the spacecraft. Fig. 2 depicts the orientations of these eight thrusters relative to the mechanical axes of the spacecraft. These eight A-branch thrusters are backed up by eight B-branch thrusters. Pointing control about the spacecraft's X and Y axes is performed using four Z-facing thrusters. Control about the Z-axis is performed using four Y-facing thrusters. Cassini's thrusters have rich heritage from the Voyager program.

The monopropellant propulsion system for Cassini is of the blow-down type. With this system, the hydrazine tank pressure will decay slowly with time as hydrazine is depleted through thruster firings. At launch (October 15, 1997), the thrust magnitude was about 0.97 N. By the time of Saturn Orbit Insertion (June 30, 2004), the thrust magnitude had decayed to 0.75 N. The monopropellant tank was "recharged" only once on June 17, 2006. In-flight characterization of the performance of the Cassini propulsion system was described in detail in Ref. 7. A thruster swap from A-branch to B-branch happened in the spring of 2009.[17]

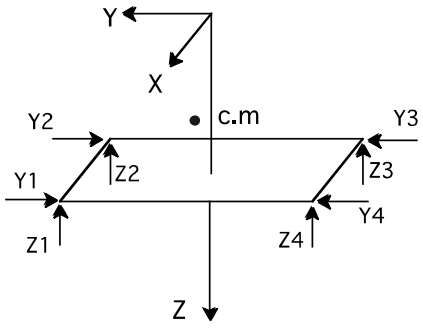

Fig. 2. Cassini Thruster Configuration[7,9]
(Arrows indicate reaction forces)

A conventional Bang-Off-Bang (BOB) thruster control algorithm is used by Cassini AACS. The BOB algorithm uses error signals that are the weighted sums of per-axis attitude errors and attitude rate errors to control thruster firings. However, such a control algorithm can result in "two-sided" limit cycles that waste both hydrazine and thruster on/off cycles. In order to counter these drawbacks, the Cassini's BOB incorporated a "self-learning" feature to produce, as much as possible, "one-sided" limit cycles in the presence of small environmental torque. The bandwidth of the RCS attitude controller is selected to be 0.15 Hz. An example of the RCS controller performance is depicted in Fig. 3 (from Ref. 8).

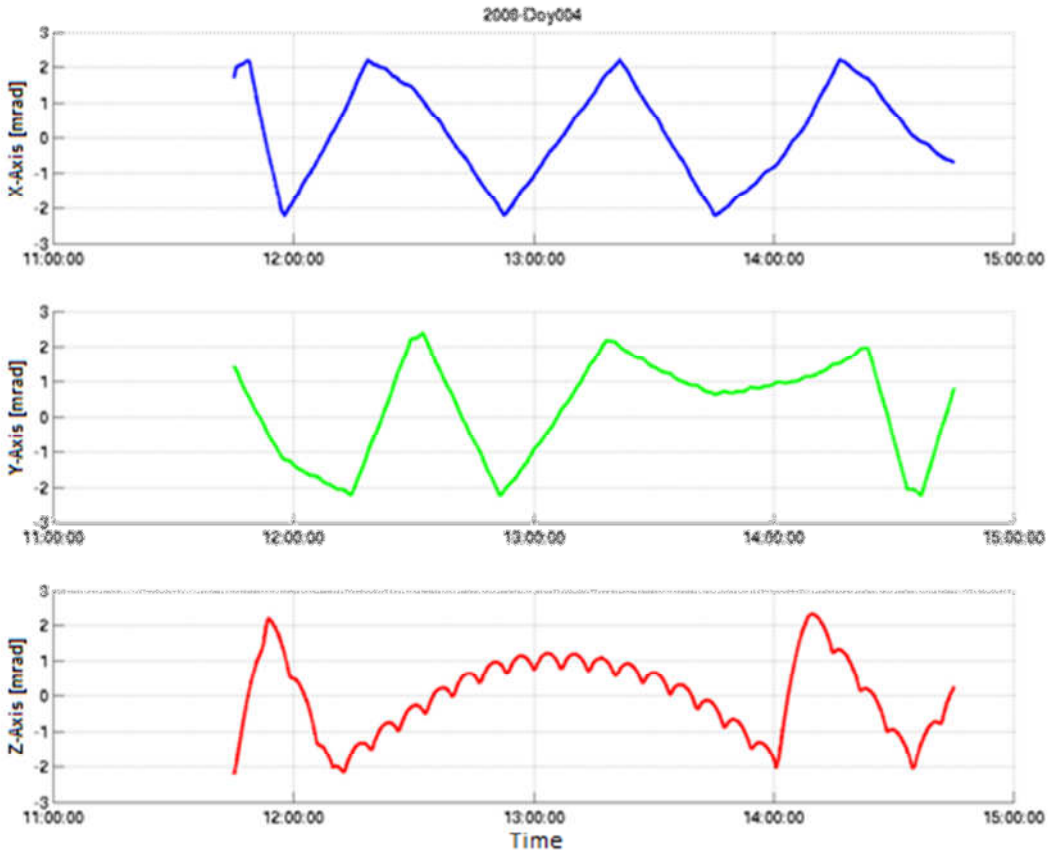

Figure 3. Time Histories of Spacecraft Per-axis Attitude Control Errors[8]

IV. Enceladus Density Reconstruction Methodologies

Three methodologies were discussed in the literature to estimate the disturbance torque imparted on the Cassini spacecraft due to either Titan atmospheric torque or Enceladus plume jets. Another methodology that is based on the Euler equation is given in this paper. They are listed in Table 2. These methodologies are briefly described in this section. Enceladus plume densities estimated using these methodologies are given in Section VI.

Table 2. Methodologies Used to Estimate Disturbance Torque Imparted on Cassini*

Method	Control Mode	S/C State	Underlying Principle of the Density Estimation Methodology	Refs.
1	RWA	Quiescent	Conservation of total angular momentum in an inertial frame	13–15
2	RWA	Slew	Use the general Euler equation	This work
3	RWA	Quiescent	Use the transfer function between attitude control error and disturbance torque	15
4	RCS	Quiescent	Conservation of total angular momentum in an inertial frame	9, 12–14

*References 9, 12, and 13 described similar methodologies that were used to reconstruct atmospheric torque imparted on Cassini during Titan flybys. Reference 14 described a similar methodology for torque estimation during Enceladus flybys.

A. Cassini is controlled by reaction wheels and is in a quiescent state during the flyby

In order to maintain a quiescent spacecraft attitude in an inertial frame, the three prime RWAs must "absorb" the angular momenta imparted on Cassini due to the (time-varying) plume torque. As a result, the RWA spin rates change as the spacecraft passed through the plume cloud. These RWA spin rate changes could be used to estimate the plume torque. To this end, we note that the total angular momentum vector of the spacecraft, expressed in the spacecraft body frame, has two components:

$$\vec{H}_{Total} = \vec{H}_{SC} + \vec{H}_{RWA}. \tag{2}$$

The component due to the spacecraft rate is:

$$\vec{H}_{SC} = I_{SC}\vec{\omega} \tag{3}$$

where the spacecraft rate vector is:

$$\vec{\omega} = [\omega_x, \omega_y, \omega_z]^T. \tag{4}$$

To determine the angular momentum of the RWAs, we first define the following expression:

$$\vec{\rho} = [\rho_1, \rho_2, \rho_4]^T \tag{5}$$

where ρ_i (i=1,2, and 4) is the spin rate of the i^{th} RWA about its spin axis. As mentioned earlier, Cassini attitude has oftentimes been controlled by the orthogonal set of reaction wheels RWA-1, RWA-2, and RWA-4 since mid-July 2003. To find $\vec{H}_{RWA}$, we first multiply $\vec{\rho}$ by the inertia matrix of the RWAs and then multiply the resultant vector by the wheel-to-spacecraft coordinate transformation matrix T.

$$\vec{H}_{RWA} = TI_{RWA}\vec{\rho} \tag{6}$$

The coordinate transformation matrix T is given in Ref. 9, and the 3×3 diagonal inertia matrix of the reaction wheels is I_{RWA} = diag(0.16138, 0.15947, 0.16138)^T kg-m^2. As an example, the resultant time history of the Z-axis angular momentum of the spacecraft during the Enceladus-3 flyby is depicted in Fig. 4.

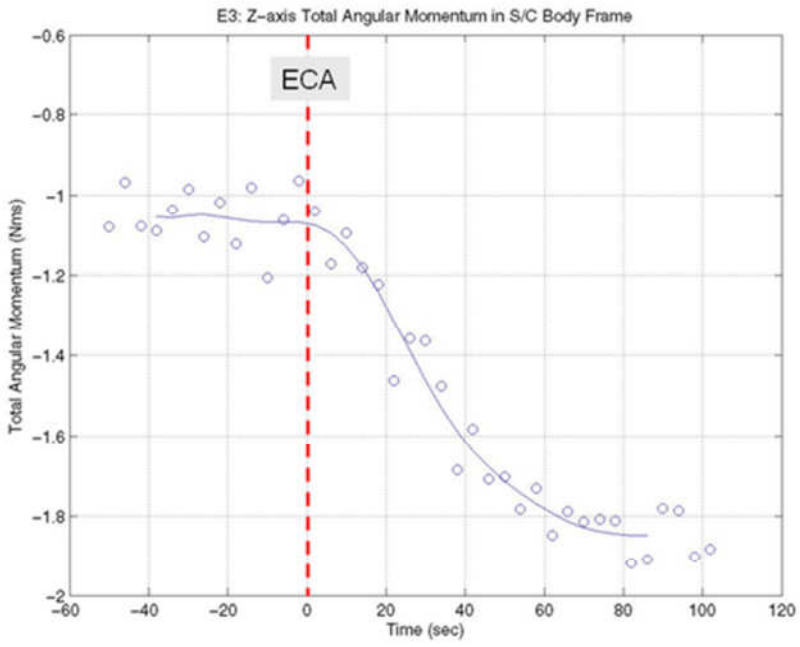

Fig. 4 Computed Z-axis Angular Momentum of Cassini During Enceladus-3 Flyby[15]

The time rates of change of the computed per-axis angular momenta are the per-axis plume torque imparted on Cassini. For the E3 flyby, the slope of the Z-axis angular momentum (as depicted in Fig. 4) is computed numerically. To this end, we first approximate the Z-axis angular momentum by a 12th order polynomial:

$$H^{Z}_{Total}(t) = \sum_{i=0}^{12} p_i t^i \tag{7}$$

Accordingly, the plume torque imparted on the spacecraft is given by:

$$T^{Z}(t) = \sum_{i=1}^{12} i p_i t^{i-1}. \tag{8}$$

With the use of a 12th order polynomial, the root-mean-square (RMS) fitting error is 0.0602 Nms. The mean value of the magnitudes of the Z-axis angular momentum data depicted in Fig. 4 is -1.432 Nms. Hence, the fitting error is about 4.23% of the mean magnitude. Higher order polynomials, for example, 15th and 18th order, will reduce the percent error from 4.23 to 3.85 and 3.71%, respectively. They were not used because the improvement isn't significant. The plume torque imparted on Cassini during the Enceladus-3 flyby is depicted in Fig. 5

.

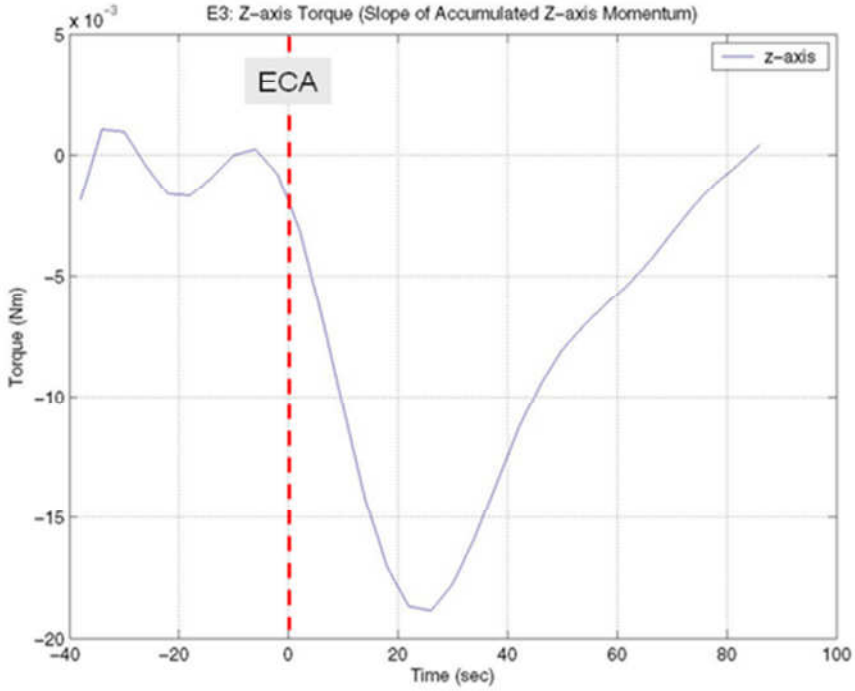

Fig. 5 Computed Z-axis Plume Torque Imparted on Cassini During Enceladus-3 Flyby[15]

B. Cassini is controlled by reaction wheels and is being slewed during the flyby

During some Enceladus flybys, the spacecraft was not in a quiescent state. For example, the spacecraft had a non-zero Z-axis body rate during the Enceladus-4 flyby. As such, the methodology described in Section IV.A could not be used directly to estimate the plume torque imparted on the spacecraft. The following methodology, a generalization of that described in Section IV.A, must be used.

Based on the Euler equation, the time rate of change of the total angular momentum of the spacecraft (see Eq. (2)) in an inertial frame is the external torque acting on the spacecraft.

$$I_{SC}\dot{\vec{\omega}} + TI_{RWA}\dot{\vec{\rho}} + \vec{\omega} \times I_{SC}\vec{\omega} + \vec{\omega} \times TI_{RWA}\vec{\rho} = \vec{M}_{External} \tag{9}$$

For the Enceladus-4 flyby, the spacecraft has non-zero rate only about the Z-axis and the largest plume torque imparted on the spacecraft was about the X-axis. Therefore, the X-axis component of Eq. (9) can be re-written as:

$$I_{XX}\dot{\omega}_X + \frac{1}{\sqrt{2}} I_{RWA}\{\dot{\rho}_{RWA4} - \dot{\rho}_{RWA2}\} + (I_{ZZ}\text{-}I_{YY})\omega_Y\omega_Z + \{\omega_Y H^Z_{RWA} - \omega_Z H^Y_{RWA}\} = M^X_{External}$$

where:

$$H^Y_{RWA} = I_{RWA}\{\sqrt{\frac{2}{3}}\omega_{RWA1} - \frac{1}{\sqrt{6}}\omega_{RWA2} - \frac{1}{\sqrt{6}}\omega_{RWA4}\} \tag{10}$$

$$H^Z_{RWA} = \frac{I_{RWA}}{\sqrt{3}}\{\omega_{RWA1} + \omega_{RWA2} + \omega_{RWA4}\}$$

In deriving Eq. (10), we have ignored all the products of inertia (e.g., I_{XY}) in I_{SC}. For Cassini, the largest product of inertia, when divided by the smallest moment of inertia, is only 3.6%. Hence, this is a reasonable simplification. Also, we have used the coordinate transformation matrix T given in Ref. 9. Having integrated both sides of the first equation in Eq. (10), we obtain the following expression:

$$I_{XX}\{\omega_X(t) - \omega_X(0)\} + \frac{1}{\sqrt{2}} I_{RWA}\{[\rho_{RWA4}(t) - \rho_{RWA4}(0)] - [\rho_{RWA2}(t) - \rho_{RWA2}(0)]\} \tag{11}$$
$$+ \int_0^t \{(I_{ZZ}\text{-}I_{YY})\omega_Y\omega_Z + \omega_Y H^Z_{RWA} - \omega_Z H^Y_{RWA}\}\,d\tau = \int_0^t M^X_{External}(\tau)\,d\tau$$

The LHS of Eq. (11) represents the changes in the X-axis angular momentum due to the X-axis plume torque. The time history of the X-axis angular momentum could be computed using the telemetry data of both the spacecraft's per-axis rates and the reaction wheel rates. Using the approach described in Section IV.A (see Eqs. (7–8)), the computed time history of the X-axis angular momentum could be fitted using a high-order polynomial. The time derivative of the polynomial is the X-axis plume torque imparted on the spacecraft. Unfortunately, since the telemetry data of reaction wheel rate were collected at a slow rate of once per four seconds during the Enceladus-4 flyby, it is relatively hard to reconstruct the small X-axis torque using a small set of wheel data. Thus, the reconstructed density, which might be incorrect, is not included in this paper.

C. Cassini is controlled by reaction wheels and is in a quiescent state during the flyby

With reference to Fig. 1, we note that in response to the attitude command $\theta_C(s)$, attitude rate command $\omega_C(s)$, attitude acceleration command $\alpha_C(s)$, and under the influence of an external disturbance torque $T_D(s)$, the spacecraft attitude $\theta(s)$ is given by:

$$\theta(s) = G_\theta(s)\theta_C(s) + G_\omega(s)\omega_C(s) + G_\alpha(s)\alpha_C(s) + G_T(s)[T_D(s) + T_{Gyroscopic}(s)] \tag{12}$$

In this expression, "s" is the Laplace operator, and the "G(s)" terms represent transfer functions from the stimuli (e.g., attitude command) to the spacecraft attitude. Without loss of generality, we consider a special case when the reaction wheels are used to maintain a quiescent spacecraft attitude during the Enceladus flyby. That is, $\theta_C = \omega_C = \alpha_C = 0$. Both the Enceladus-3 and Enceladus-9 flybys satisfy these conditions. Since the spacecraft rate vector is zero, the gyroscopic term in Eq. (12) is also zero. From Ref. 10, the transfer function between the disturbance torque $T_D(s)$ and the attitude control error $e_\theta(s)$ is given by:

$$\frac{e_\theta(s)}{T_D(s)} = -\frac{(s^2 + 2\xi\omega s + \omega^2)^2 / I_{SC}}{Den(s)} \tag{13}$$

The denominator of the term on the RHS of Eq. (13) is given by:

$$\begin{aligned} Den(s) = {} & s^6 + 4\xi\omega s^5 + (4\omega^2\xi^2 + 2\omega^2 + 4K_PK_D)s^4 + \\ & (4\omega^3\xi + 4K_PK_D\omega\xi)s^3 + (\omega^4 + 4K_PK_D\omega^2\xi^2 + 2K_PK_D\omega^2)s^2 + \\ & (K_D\omega^4 + 4K_PK_D\omega^3\xi)s + K_PK_D\omega^4 \end{aligned} \tag{14}$$

In Eqs. (13–14), the natural frequency (ω) and damping coefficient (ξ) of the 4th order low-pass filter (depicted in Fig. 1) are 2.34048 rad/s and 0.4000, respectively. The proportional (K_P) and derivative (K_D) gains of the RWA controller are given by: $K_P = \omega_n/(2\xi_n)$, and $K_D = 2\omega_n\xi_n$. Here, $\omega_n = 2\pi\times0.0299$ rad/s (RWAC bandwidth), and $\xi_n = 0.4138$ (dimensionless). Note that the bandwidth of the RWA controller is about an order of magnitude lower than the center frequency of the low-pass filter. For simplicity, we derive a low-order transfer function of Eq. (13) by ignoring the 4th order low-pass filter:

$$\frac{e_\theta(s)}{T_D(s)} = -\frac{1/I_{SC}}{s^2 + K_D s + K_P K_D} = -\frac{1/I_{SC}}{s^2 + 2\xi_n\omega_n s + \omega_n^2} = -\frac{0.0002747}{s^2 + 0.15548 s + 0.03529} \tag{15}$$

From this equation, one can estimate the disturbance torque using the inverse Laplace transformation of Eq. (15) to be:

$$T_D(t) \approx -3640.4\{\ddot{e}_\theta(t) + 0.15548\dot{e}_\theta(t) + 0.03529 e_\theta(t)\} \text{ Nm} \tag{16}$$

In Eq. (16), the attitude control error $e_\theta(t)$, in radians, is given by the per-axis attitude control errors.[15] The term $\dot{e}_\theta(t)$ in Eq. (16), in rad/s, is computed using both the attitude control errors and the attitude rate control errors. Next, 6th order polynomials such as that given in Eq. (17) below are used to generate "smoothed" versions of these telemetry data. For example, the Z-axis attitude control error telemetry data (channel A-1182) is approximated by:

$$A_{1182}(t) = \sum_{i=0}^{6} k_i t^i \tag{17}$$

The "smoothed" telemetry data are then used to estimate $e_\theta(t)$, $\dot{e}_\theta(t)$, and $\ddot{e}_\theta(t)$. Finally, the disturbance torque is computed via Eq. (16).

Subsequently, there is another way to obtain the reduced-order transfer function of Eq. (13). The Hankel singular values of a transfer function measure the contribution of each state to the input/output behavior of the system. States with small Hankel singular values indicate that they have limited contribution to the input-output mapping of the transfer function and are candidates for deletion. In this study, we use the *Model Reduction Toolbox* of MATLAB© to perform the needed computations. Four system "states" are deleted and the 6th order transfer function becomes a 2nd order transfer function:

$$\frac{e_\theta(s)}{T_D(s)} = -\frac{0.0003091}{s^2 + 0.1753 s + 0.03977}$$
$$T_D^Z(t) \approx -\frac{1}{0.0003091}\{\ddot{e}_\theta(t) + 0.1753\dot{e}_\theta(t) + 0.03977 e_\theta(t)\} \text{ Nm} \tag{18}$$

A comparison of the frequency responses of the full and reduced-order transfer function is depicted in Fig. 6. Clearly, the second-order transfer function Eq. (18) approximates the full-order transfer function quite well. Thus, it is used in our study.

D. Cassini is controlled by RCS thrusters and is in a quiescent state during the flyby

Cassini was controlled by thrusters during many low-altitude Titan flybys and several low-altitude Enceladus flybys. The thrusters were fired to overcome the atmospheric torque imparted on the spacecraft due to the Titan atmosphere (or Enceladus plume jets). In all these flybys, the reaction wheels were powered off. Having all the reaction wheels powered off, no thruster firing is needed to counter any gyroscopic torque due to spinning reaction wheels. Obviously, the denser Titan's atmosphere (or Enceladus' plume jets) is, the more thruster firings will be needed. In other words, thruster firing telemetry data could be used to estimate the three axis torque imparted on the spacecraft due to the plume jets. Again, we note that the rotational motion of the spacecraft during an Enceladus flyby is governed by the Euler equation:

$$I_{SC}\dot{\vec{\omega}} + \vec{\omega}\times I_{SC}\vec{\omega} = \vec{T}_{PMS} + \vec{M}_{Plume} + \vec{\varepsilon} \tag{19}$$

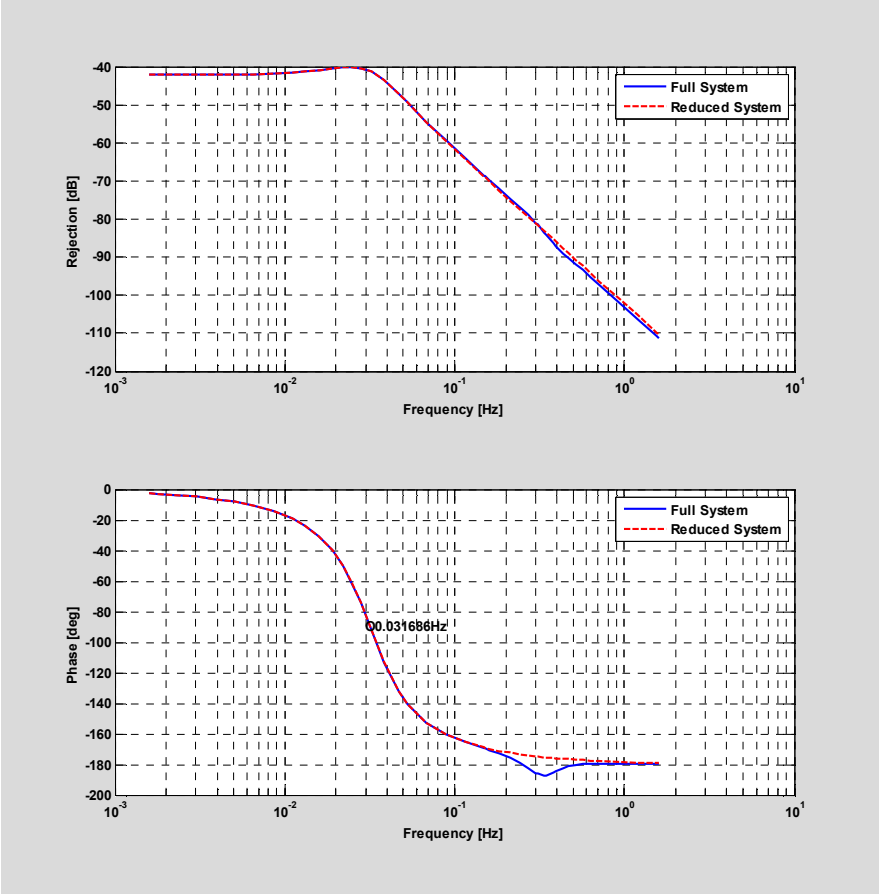

Fig. 6. Frequency Responses of the Full-order and Reduced-order Models

In Eq. (19), I_{SC} is the S/C's inertia tensor, the spacecraft angular rate vector is $\vec{\omega}$, and the spacecraft's angular acceleration vector is $\dot{\vec{\omega}}$. The on-board attitude estimator provides estimates of the spacecraft attitude rate. Torque exerted on the spacecraft due to thruster firing, $\vec{T}_{PMS}$, is not available directly from telemetry data. Instead, the accumulated thrusters' on-time of all the thrusters is available. Using the estimated thruster moment arms and thrusters' magnitude, one can estimate the time histories of the per-axis torque impulses. Torque exerted on the spacecraft due to the Enceladus plume jet density is denoted by $\vec{M}_{Plume}$. Environmental torque such as the Enceladus' gravity gradient torque is captured in the "ε" term. This torque is typically very small and is neglected (also see Section V).

In many thruster-based Enceladus flybys (e.g., both the Enceladus-5 and 7 flybys), the spacecraft maintained a quiescent attitude throughout the flyby. As such, the gyroscopic term on the LHS of Eq. (19) is nearly zero. Furthermore, in both Enceladus flybys, the angular momentum imparted on the spacecraft due to the Enceladus plume was mainly about the S/C's Z-axis. Hence, we have:

$$\int_0^t M^Z_{Plume}(\tau)d\tau = I_{ZX}\Delta\omega_X(t)+I_{ZY}\Delta\omega_Y(t)+I_{ZZ}\Delta\omega_Z(t)... \\ -F_{PMS}L_{PMS}\{f^{Y2Y4}_{Dynamics}[\Delta\tau^{Y2}(t)+\Delta\tau^{Y4}(t)]-f^{Y1Y3}_{Dynamics}[\Delta\tau^{Y1}(t)+\Delta\tau^{Y3}(t)]\} \quad (20)$$

With reference to Fig. 2, we see that in order to counter disturbance torque about the minus Z-axis of the spacecraft, both Y_2 and Y_4 thrusters must be fired as a pair. Similarly, to counter disturbance torque about the Z-axis, both Y_1 and Y_3 thrusters must be fired as a pair. Hence, the on-times of these Y-facing thrusters must all be

accounted for in Eq. (20). In Eq. (20), F_{PMS} denotes the magnitude of these Y-facing thrusters, and $\Delta\tau^{Yi}$ denotes the accumulated on-times of thruster Y_i (relative to a reference time just before the spacecraft entered the plume jets). The coordinates of the four Y-facing thrusters, Y_1, Y_2, Y_3, and Y_4 are given by: $[+L_X, +L_Y, +L_{ZY}]$, $[-L_X, +L_Y, +L_{ZY}]$, $[-L_X, -L_Y, +L_{ZY}]$, and $[+L_X, -L_Y, +L_{ZY}]$, respectively (from Ref. 12, see also Fig. 2). Approximately, $L_X = 1.234$ m, $L_Y = 1.580$ m, and $L_{ZY} = 2.880$ m. Let the vector $[e_X, e_Y, e_Z]^T$ denotes the coordinates of the S/C's center of mass. The moment arm matrix Q (3×4), from the four thrusters Y_1, Y_2, Y_3, and Y_4 to the three S/C's coordinate axes is given by:[16]

$$Q = \begin{bmatrix} +(L_{ZY}-e_Z) & +(L_{ZY}-e_Z) & -(L_{ZY}-e_Z) & -(L_{ZY}-e_Z) \\ 0 & 0 & 0 & 0 \\ -(L_X-e_X) & +L_X+e_X & -L_X-e_X & +L_X-e_X \end{bmatrix} \tag{21}$$

With reference to the third row of Eq. (21), we note that since thrusters $[Y_1, Y_3]$ and $[Y_2, Y_4]$ always fired as pairs, the quantity e_X does not enter the calculations of the Z-axis angular momentum. Also, $L_{PMS} = L_X = 1.234$ m. For simplicity, a single thruster magnitude F_{PMS} is assumed for the four Y-facing thrusters. The correction factor $f_{Dynamics}$ is explained below.

The dynamics of a thruster valve is typically modeled with both "rise" and "fall" exponential time constants τ_R and τ_F, respectively. The thrust profile with assumed values of τ_F equal to 65 msec and τ_R equal to 20 msec is depicted in Fig. 7. Note that, since the fall time constant is typically longer than the rise time constant, the net area under the thrust profile (impulse) is larger than the "rectangular" impulse. Let the <u>mean</u> on-time of the thruster pair (Y_1/Y_3 or Y_2/Y_4) used during the spacecraft passage through the Enceladus plume be Δ s. The total area under the thrust curve is:[16–17]

$$\begin{aligned} \text{Thrust Impulse [Ns]} &= F_{PMS}(\Delta+\tau_F) + F_{PMS}\tau_R\{e^{-\frac{\Delta}{\tau_R}}-1\} - F_{PMS}\tau_F e^{-\frac{\Delta}{\tau_R}} \\ &= F_{PMS}\{\Delta + (1-e^{-\frac{\Delta}{\tau_R}})(\tau_F-\tau_R)\} \end{aligned} \tag{22}$$

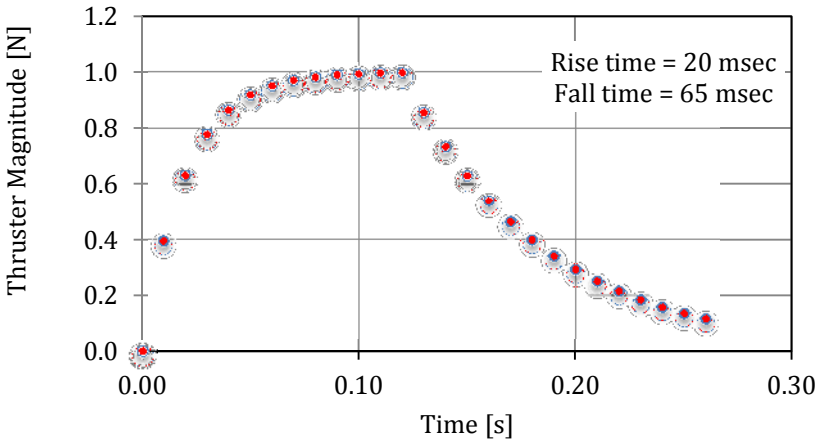

Fig. 7. Rise and Fall Dynamics of Thruster Impulse

Accordingly, the factor $f_{Dyanmics}$ in Eq. (20) is given by:

$$\begin{aligned} f_{Dynamics} &= F_{PMS}\{\Delta + (1-e^{-\frac{\Delta}{\tau_R}})(\tau_F-\tau_R)\} \div F_{PMS}\Delta \\ &= 1+(1-e^{-\frac{\Delta}{\tau_R}})\{\frac{\tau_F-\tau_R}{\Delta}\} \end{aligned} \tag{23}$$

Estimated thruster characteristics for the E5 and E7 flybys are given in Table 3. The $f_{Dynamics}$ for the thruster pairs Y1/Y3 and Y2/Y4 could then be computed using Eq. (23). With these estimated parameters, the angular momentum imparted on the spacecraft due to the Enceladus plume could be estimated via Eq. (20). The time derivative of the Z-axis angular momentum can then approximate the Z-axis plume torque imparted on the spacecraft because the torque from thrusters is equal and opposite to the torque from the plume.

Table 3. Thruster Characteristics Used in This Study for the E5 and E7 Flybys

Enceladus Flyby	Thruster Branch Used	Mean Thruster Magnitude[#] [N]	Rise Time Constant [msec]	Fall Time Constant[†] [msec]	Average Y_1/Y_3 Thruster On-time* [msec]	Average Y_2/Y_4 Thruster On-time* [msec]
5	A	0.80	20	52	121	74
7	B	0.77	20	39	63	48

[#]For these flybys, the plume torque was mainly about the S/C's Z-axis. Hence, as per Fig. 2, Y-facing thrusters were used to counter them. Thruster magnitudes given here correspond to these Y-facing thrusters.
[†]From Reference 17.
*From E5 and E7 telemetry data.

V. Reconstructed Density of Enceladus Plume Clouds

The Enceladus plume density is related to the torque imparted on the spacecraft by the following approximate relation:[9,12–15]

$$\vec{T}_{Plume}(t) = -\frac{1}{2} C_D \rho_{Plume}(t) V(t)^2 A_{Project}(t) \vec{u}_V(t) \times [\vec{r}_{CP}(t) - \vec{r}_{CM}(t)] \tag{24}$$

In this equation, $T_{Plume}(t)$ is the torque imparted on the spacecraft that was estimated using one of the methodologies described in Section IV. The time history of the Enceladus plume density, in kg/m^3, is denoted by $\rho_{Plume}(t)$. The spacecraft velocity relative to Enceladus is denoted by V(t) (in m/s), and is estimated by the Cassini Navigation team. The unit vector of the S/C's velocity vector expressed in the S/C's coordinate frame is $\vec{u}_v(t)$. The projected area of the spacecraft is $A_{Project}$ (in m^2), and the displacement vectors from the origin of the spacecraft coordinate frame to the spacecraft's center of mass and to the center of pressure (in meters) are denoted by $\vec{r}_{CM}(t)$ and $\vec{r}_{CP}(t)$, respectively. Both vectors and the projected area are estimated by a ground software tool. Finally, C_D, the drag coefficient associated with the free molecular flow of Enceladus' plume constituents past the Cassini spacecraft, was known from past research: $C_D \approx 2.1 \pm 0.1$.[9] As an example, for Enceladus-3, V = 14.41 km/s (cf. Table 1), $A_{Project}$ = 18.401 m^2, and the Z-axis moment arm of the cm-to-cp vector = 0.853 m. Accordingly,

$$\vec{T}_{Plume}(t)\ [\text{Nm}] = 3.422 \times 10^{+9} \rho_{Plume}(t) \tag{25}$$

Given the known time history of the plume torque, the plume density could be computed accordingly. The uncertainty of the estimated Enceladus plume density could be computed as follows:

$$\left[\frac{\sigma_\rho}{\rho}\right]^2 = \left[\frac{\sigma_{T_{PLUME}}}{T_{PLUME}}\right]^2 + \left[\frac{\sigma_{C_D}}{C_D}\right]^2 + 4 \times \left[\frac{\sigma_V}{V}\right]^2 + \left[\frac{\sigma_{A_{Projected}}}{A_{Projected}} + \frac{\sigma_{r_{cpcm}}}{r_{cpcm}}\right]^2 \tag{26}$$

In this expression, σ_S represents the one-sigma estimation uncertainty of "S" (e.g., the drag coefficient, C_D). All quantities on the right-hand-side of Eq. (26) are assumed to be uncorrelated. Hence, the variances of the normalized quantities are added together algebraically to produce the variance of the normalized plume density. However, we did assume that the estimation uncertainties of the spacecraft projected area and the cm-to-cp offset distance are fully correlated. Accordingly, the "σ" of these two normalized quantities are first added together before the sum is squared to produce the variance. The factor "4" in front of $[\sigma_V/V]^2$ was introduced to account for the fact that $\partial\rho/\partial V = 2$. The combined 1σ estimation uncertainty of knowledge errors of C_D, V, $A_{project}$, and the cm-to-cp offset distance

in Eq. (26) is 3.05%.[12] The overall 1σ uncertainty of the estimated density is the RSS of 3.05% and the 1σ uncertainty of the estimated torque. The latter depends on the reconstruction methodology employed. For methodologies described in both Sections IV.A and IV.C, the 1σ uncertainty of the estimated torque is 5%.[15] Hence, the 1σ uncertainty of the estimated plume density is RSS(5,3.05) = 5.9%. For the methodologies described in Section IV.B and IV.D, the 1σ uncertainty of the estimated torque is judged to be 6%.[‡] As such, the 1σ uncertainty of the estimated plume density is 6.7%.

One other "disturbance" torque imparted on the spacecraft during an Enceladus flyby is the gravity gradient torque. The magnitude of gravity gradient torque is a function of both spacecraft attitude and its distance from Enceladus. With a worst-case spacecraft attitude, this torque could be estimated using the following expression:

$$T_{Gravity-Gradient} = \frac{3}{2}\mu_{Enceladus}\frac{(I_{Max} - I_{Min})}{(R_{Enceladus} + h)^3} \tag{27}$$

Here, $\mu_{Enceladus}$ is the product of the universal gravitational constant and the mass of Enceladus (≈7.207±0.011 km^3/s^2),[11] $R_{Enceladus}$ is the effective radius of Enceladus (≈ 252.3±0.2 km),[1,11] h is the spacecraft's Enceladus-relative altitude at the time the torque peaked (322.3 km for the Enceladus-3 flyby), and I_{Max} and I_{Min} are the maximum and minimum moments of inertia of the spacecraft, respectively. The *worst-case* magnitude of $T_{Gravity-Gradient}$ is about 190 μNm which is less than 1% of the estimated peak Z-axis torque for the Enceladus-3 flyby.

From Ref. 9, the estimated magnitude of the solar radiation torque imparted on Cassini is bounded by 2 μNm, and the radiation torque imparted on the spacecraft due to the Cassini power generators is bounded by 1.83 μNm. These disturbance torques are very small. Magnetic torque acting on the spacecraft is a result of the interaction of the spacecraft's residual magnetic field and the magnetic field of Saturn at Enceladus. The magnetic disturbance torque, $T_{Magnetic}$, could be estimated using the following expression:

$$T_{Magnetic} = M_{arm} \times B_{Enceladus} \tag{28}$$

Here, M_{arm} is the spacecraft magnetic moment arm, estimated to be 1.4 Amp-m^2, and $B_{Enceladus}$ is the magnetic flux density of Saturn at Enceladus. Enceladus is located in the inner magnetosphere of Saturn at a radial distance of 3.94 R_S (1 R_S = 60,268 km). The magnetic field strength in this region is ≈ 320 nT (nano-Telsa, Tesla = kg-s^{-2}-A^{-1}). It is also estimated that the Enceladus plume has at most a 10% impact on the magnetic flux density. Accordingly, the estimated worst-case magnitude of $T_{Magnetic}$ is 0.5 μNm. Since the gravity gradient torque, solar radiation torque, radiation torque due to power generators, and magnetic torque are all insignificant, the estimated torque imparted on the spacecraft is assumed to be solely due to the watery plume.

[‡]The 1σ estimation uncertainty of the disturbance torque reconstructed using the methodology described in Section IV.D was judged to be 4% in Ref. 14. A larger uncertainty is used in this study. The difficulty associated with the estimations of thrusters' rise and fall time constants was not accounted for in Ref. 14.

VI. Reconstructed Plume Density and Discussions

The projected views of the E3, E5, E7, and E9 flybys on a plane formed by the spacecraft trajectory and the North-South axis of Enceladus are depicted in Figs. 8, 9, 11, and 12, respectively. These projected views were drawn to scale. The dark lines in these figures depict Cassini's flyby trajectories, and the "+" represents the locations where Cassini experienced the peak plume torque. Another set of projected views of these flybys is given in Fig. 14. In this set of views, the flyby trajectory is projected on the equatorial plane of Enceladus. From these projections, we can identify the key plume sources over which Cassini flew passed in each flyby. The longitudes and latitudes of the plume sources are tabulated in Table 4. The offset distances of these plume sources from the projected trajectories of the Enceladus flybys are given in Table 5.

Table 4. Locations of Key Plume Sources that Impacted Cassini During Enceladus Flybys Studied[3]

Plume Sources	Alexandria IV	Cairo VIII	Damascus II	Damascus III	Baghdad VI
South latitude (γ_{LAT}), deg	72.9	82.1	79.4	81.3	87.1
West longitude (γ_{LON}), deg	148.7	115.5	315.5	292.8	231.4

Table 5. Offset distances of Key Plume Sources from the Projected Trajectories of Four Enceladus Flybys Studied in this Work (see also Fig. 14)

Flyby	Offset distance of Plume Source from Projected Trajectory [km]*				
	Alexandria IV	Cairo VIII	Damascus II	Damascus III	Baghdad VI
E3	11.4	17.8	5.8	8.2	6.5
E5	57.4	10.4	28.2	9.7	9.3
E7	13.3	23.9	18.5	27.5	12.2
E9	2.2	18.1	9.3	21.4	12.7

*Offset distance $\approx \|\|R_{Enceladus}\cos(\gamma_{LAT})\sin(\beta_{LON}-\gamma_{LON})\|\|$, where β_{LON} and γ_{LON} were defined in Tables 1 and 4, respectively.

For Enceladus-3, the peak density estimated using the transfer function approach (Table 2, Method 3) is 5.49×10^{-12} kg/m^3 (Fig. 10). For Enceladus-5, the peak density estimated using the conservation of total angular momentum approach (Table 2, Method 4) is 1.12×10^{-11} kg/m^3 (also given in Fig. 10). For Enceladus-7, the peak density estimated using the conservation of total angular momentum approach (Table 2, Method 4) is 3.11×10^{-11} kg/m^3 (Fig. 13). For Enceladus-9, the peak density estimated using the conservation of total angular momentum approach (Table 2, Method 1) is 34.7×10^{-12} kg/m^3 (also given in Fig. 13). These results are summarized in Table 6.

Table 6. Estimated Enceladus Plume Density

Flyby	Date of Flyby And ECA Time	ECA Altitude [km]	Spacecraft Control Mode	Peak Density (10^{-12} kg/m^3)	1σ Density Estimation Uncertainty (%)
E3	03/12/2008T19:06:12	47.9	RWA	5.49	5.9
E5	10/09/2008T19:06:40	28.98	RCS (A-branch)	11.2	6.7
E7	11/02/2009T07:41:58	102.69	RCS (B-branch)	31.1	6.7
E9	04/28/2010T00:10:17	102.7	RWA	34.7	5.9

The locations where the spacecraft experienced the largest disturbance torque are marked by "+" in Figs. 8–9 and 11–12. With reference to Fig. 10 and Table 7, we note that the peak Enceladus plume density experienced by the spacecraft during the E5 flyby is about a factor of 2.04 larger than its E3 counterpart. In the following, we use the simple Enceladus plume density model proposed in Ref. 15 to explain this result. The density model proposed in Ref. 15 is:

$$\rho(r,\theta) = K[\frac{R_E}{r}]^{\frac{3}{2}} e^{-\frac{\theta}{D}} \tag{29}$$

In this equation, r (in km) is the distance between the spacecraft and the plume source (e.g., Cairo VIII), and R_E is the radius of Enceladus (252 km). To avoid a singularity at r = 0, we will restrict the use of Eq. (29) to $1{,}400 \geq r \geq 50$ km. A relation $\rho \sim 1/r$ was used in Ref. 18 to model the dependency of the intensity of the dust jets from Comet 19P/Borrelly with the distance between the spacecraft and the comet. A relation $\rho \sim 1/r^2$ was used in Refs. 14 and 19 to model the dependency of the Enceladus plume jet density with distance. In this work, the relation $\rho \sim 1/r^{1.5}$ is used.[15] In all cases, the plume density is inversely proportional to the radial distance of the spacecraft from the plume source. The angular distance θ, in degrees, is the angle between the "plume source-to-spacecraft" vector and the axis of symmetry of the plume jet. The exponential constant is about 20°.[15] The "strength" of the plume source is represented by K, in units of kg/m^3. The strength's of the plume sources (e.g., Cairo VII) are assumed identical in this study.[14]

For the E3 flyby, Cassini was over Cairo VIII at the time when the disturbance torque peaked. As depicted in Fig. 8, the spacecraft was located 14.3° off the cone axis of Cairo VIII (α) and a distance of 271 km (d) at that time. In the direction that is perpendicular to axes depicted in Fig. 8, the spacecraft has an offset distance of 17.8 km (Table 5, Δ). Hence, the total offset angle of spacecraft from the plume axis of Cairo VIII (θ) and the total distance (r) are given by:

$$\text{Total off axis angle}\,(\theta) = \tan^{-1}\left\{\frac{\sqrt{(d\sin\alpha)^2 + \Delta^2}}{d\cos\alpha}\right\} = 14.8^\circ$$
$$\text{Total distance to plume source}\,(r) = \sqrt{d^2 + \Delta^2} = 273\,\text{km} \tag{30}$$

The total offset angle, the distance to the plume source Cairo VIII, and other key plume sources are listed in Table 7.

Table 7. S/C Locations where Peak Density was detected

Flyby	ECA Altitude [km]	Peak Density [10^{-12} kg/m^3]	Key Plume Source(s) that Contributed to the Peak Disturbance (See also Fig. 16) {r, θ}		
			Primary	Secondary	Third
E3	47.9	5.49	Cairo VIII {273 km, 14.8°}	Baghdad VI {280 km, 23.8°}	-
E5	28.98	11.2	Baghdad VI {338 km, 4.5°}	Cairo VIII {341 km, 13°}	Damascus III {341 km, 16°}
E7	102.69	31.1	Cairo VIII {106 km, 13.2°}	Damascus III {135 km, 48.8°}	Baghdad VI {106 km, 16.5°}
E9	102.7	34.7	Baghdad VI {104 km, 8.3°}	Cairo VIII {109 km, 23.2°}	Damascus III {118 km, 34.4°}

For the E5 flyby, Cassini was affected mainly by the plume sources Baghdad VI, Cairo VIII, and Damascus III at the time the disturbance torque peaked. The total offset angle of spacecraft from the plume axes of the key plume sources (θ) and the distances (r) are also given in Table 7. If we assume the strength of the all plume sources to be identical, then the ratio of E5 and E3 peak densities is:

$$\frac{\rho_{E5}}{\rho_{E3}} = \frac{\left\{\frac{252}{338}\right\}^{1.5} e^{-\frac{4.5}{20}} + \left\{\frac{252}{341}\right\}^{1.5} e^{-\frac{13}{20}} + \left\{\frac{252}{341}\right\}^{1.5} e^{-\frac{16}{20}}}{\left\{\frac{252}{273}\right\}^{1.5} e^{-\frac{14.8}{20}} + \left\{\frac{252}{280}\right\}^{1.5} e^{-\frac{23.8}{20}}} = \frac{1.13}{0.68} \approx 1.66 \tag{31}$$

This computed density ratio approximates that computed using density estimates given in Table 7, which is 2.04. During the E5 flyby, the closeness of the spacecraft to the cone axis of Baghdad VI and the fact that the spacecraft was under the influence of three plume sources are the main reasons why the peak density detected in this flyby is larger than its E3 counterpart.

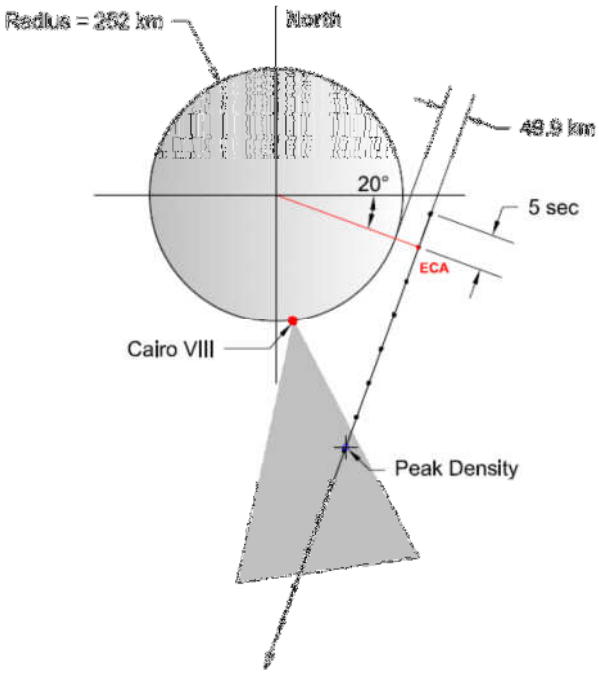

Fig. 8. Enceladus-3 Flyby

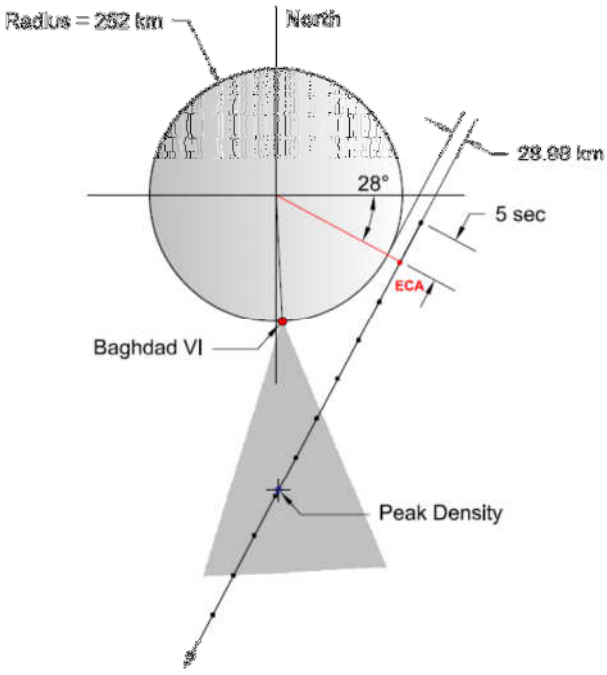

Fig. 9. Enceladus-5 Flyby

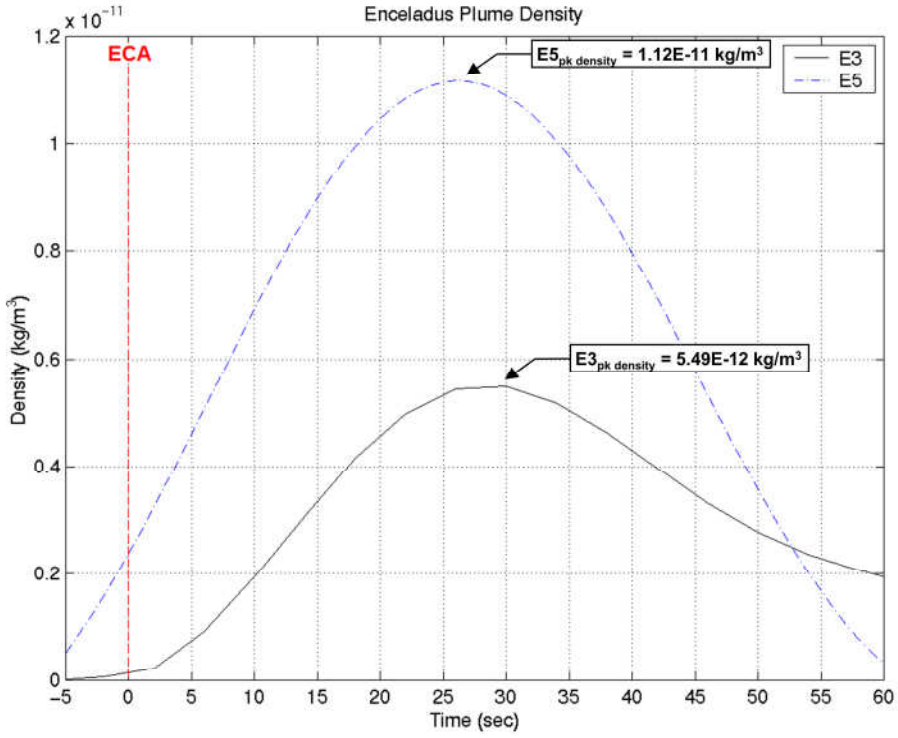

Fig. 10. Computed Enceladus Plume Density for Enceladus-3 and Enceladus-5 flybys, respectively

For the E7 and E9 flybys, Cassini experienced the largest disturbance when it was over the plume sources Cairo VIII, Baghdad VI, and Damascus III as indicated in Table 7. The ratio of peak plume densities estimated using the E5 and E7 telemetry data (given in Table 7) is 0.36. The ratio of E5 to E7 peak densities computed by the plume model is 0.30 (see Eq. (32)). They match each other quite well.

$$\frac{\rho_{E5}}{\rho_{E7}} = \frac{\{\frac{252}{338}\}^{1.5} e^{-\frac{4.5}{20}} + \{\frac{252}{341}\}^{1.5} e^{-\frac{13}{20}} + \{\frac{252}{341}\}^{1.5} e^{-\frac{16}{20}}}{\{\frac{252}{106}\}^{1.5} e^{-\frac{13.2}{20}} + \{\frac{252}{135}\}^{1.5} e^{-\frac{48.8}{20}} + \{\frac{252}{106}\}^{1.5} e^{-\frac{16.5}{20}}} = \frac{1.13}{3.72} \approx 0.30 \tag{32}$$

The ratio of peak plume densities estimated using the E7 and E9 telemetry data (given in Table 7) is 0.896. The ratio of E7 to E9 peak densities computed by the plume model is 0.9 (see Eq. (33)). This model-based density ratio matches that of computed by the reconstructed densities very well. The ratio of peak densities for the E3 and E7 flybys (given in Table 7) is 0.177. The model-based density ratio is 0.183. Again, the match is good.

$$\frac{\rho_{E7}}{\rho_{E9}} = \frac{\{\frac{252}{106}\}^{1.5} e^{-\frac{13.2}{20}} + \{\frac{252}{135}\}^{1.5} e^{-\frac{48.8}{20}} + \{\frac{252}{106}\}^{1.5} e^{-\frac{16.5}{20}}}{\{\frac{252}{104}\}^{1.5} e^{-\frac{8.3}{20}} + \{\frac{252}{109}\}^{1.5} e^{-\frac{23.2}{20}} + \{\frac{252}{118}\}^{1.5} e^{-\frac{34.4}{20}}} = \frac{3.72}{4.15} \approx 0.90 \tag{33}$$

A summary of the peak plume density ratios is given in Table 8.

Table 8. Ratios of Peak Enceladus Plume Densities Experienced in Four Flybys

Density Ratios	Density Ratios As Computed By:		Remarks
	Estimated Densities	Plume Model	
E5 / E3	2.04	1.66	Estimation uncertainties of plume densities and the use of incorrect plume model parameter values might have contributed to the mismatch
E5 / E7	0.36	0.30	Good match
E7 / E9	0.896	0.90	Good match
E3 / E7	0.177	0.183	Good match

The RMS value of the plume density parameter K (see Eq. (29)) that best fits the telemetry data from the four Enceladus flybys studied is given in Eq. (34). The RMS value of K_{RMS} is 8.41e-12 kg/m^3. This value is applicable to each one of the following three plume sources: Cairo VIII, Baghdad VI, and Damascus III. This value closely approximates those reported in Ref. 15: K (for Damascus III) is 8.5e-12 kg/m^3, and K (for Cairo VIII) is 10.3e-12 kg/m^3.

$$\begin{aligned} &\vec{\rho} = [5.5, 11.2, 31.1, 34.7]^T \ [10^{-12} \text{ kg/m}^3] \quad \text{(see Table 7)} \\ &\vec{C} = [0.68, 1.13, 3.72, 4.15]^T \ [\text{-}] \quad \text{(see Eqs. (31) – (33))} \\ &K_{RMS} = [\vec{C}^T \vec{C}]^{-1} \vec{C}^T \vec{\rho} = 8.41 \times 10^{-12} \ [\text{kg/m}^3] \end{aligned} \tag{34}$$

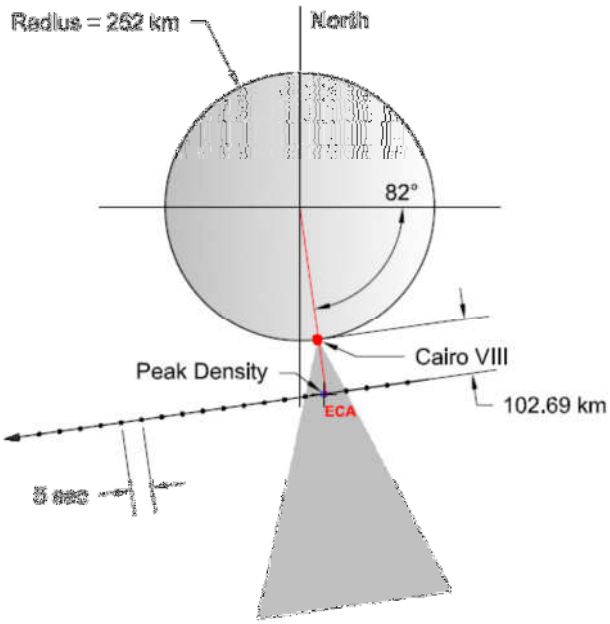

Fig. 11. Enceladus-7 Flyby

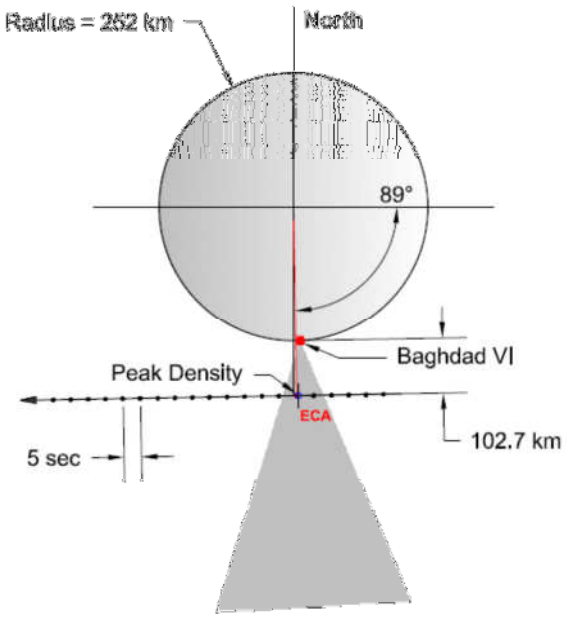

Fig. 12. Enceladus-9 Flyby

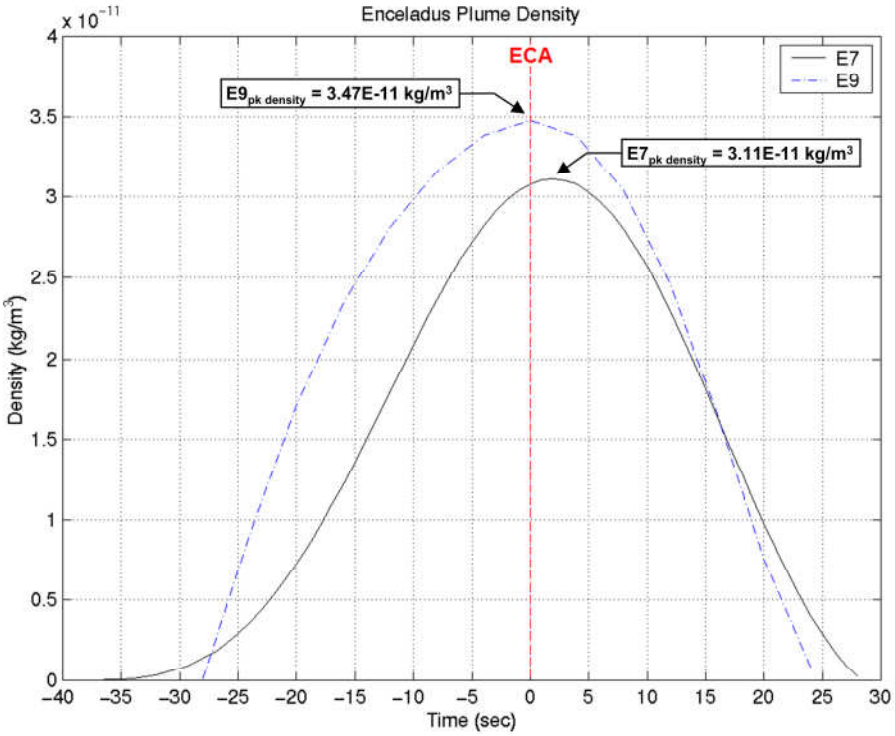

Fig. 13. Computed Enceladus Plume Density for E7 and E9 Flybys

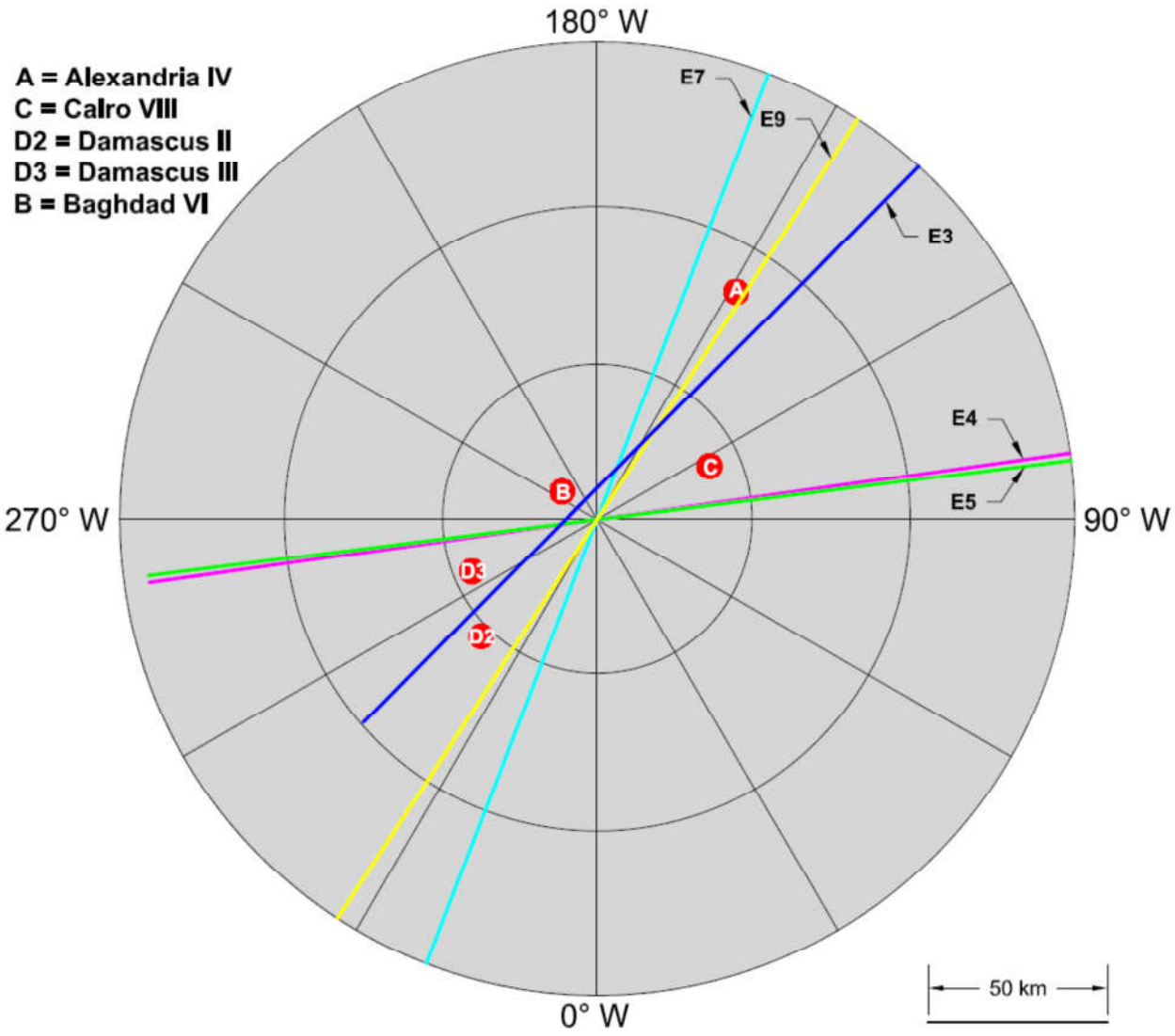

Fig.14. Enceladus Flyby Trajectories Projected on the Equatorial Plane of Enceladus (see also Appendix A)

VII. Conclusions

Using telemetry data of reaction wheel rates or thruster on-times collected from four low-altitude Enceladus flybys (E3, E5, E7, and E9), we reconstructed the time histories of the Enceladus plume jet density. The ECA altitudes of these flybys range from 29 to 102.7 km. The range of estimated peak density is 5.49–34.7e-12 kg/m^3. The 1σ uncertainty of the estimated density is 5.9–6.7% (depending on the estimation methodology employed). The estimation uncertainty of the plume density is quite large because of the large estimation uncertainty of the plume torque imparted on the spacecraft. For thruster-based flybys (E5 and E7), accurate torque is hard to estimate because of knowledge uncertainties associated with the rise and tail-off time constants of the thrusters as well as the thruster magnitude. For wheel-based flybys (E3 and E9), accurate torque imparted on the spacecraft is hard to estimate because of the slow telemetry frequencies of the reaction wheel rates and spacecraft per-axis slew rates. Increases in these telemetry frequencies in future wheel-based Enceladus flybys will be helpful for density estimation. Nevertheless, all the estimated densities fit the plume density model proposed in Ref. 15 quite well. These plume density estimates could also be used to confirm density measurements made by other onboard science instruments. Future analysis of plume densities estimated via science and engineering data collected from other low-altitude

Enceladus flybys will help to unlock the mystery behind the complex but interesting structure of the Enceladus plume.

Acknowledgments

The work described in this paper was carried out by the Jet Propulsion Laboratory, California Institute of Technology, under contract with the National Aeronautics and Space Administration. Reference to any specific commercial product, process, or service by trade name, trademark, manufacturer, or otherwise, does not constitute or imply its endorsement by the United States Government or the Jet Propulsion Laboratory, California Institute of Technology. Todd Barber, David Bates, Kathy Garcia, Cliff Lee, and Ryan Lim, our colleagues at JPL, had provided us with helpful supports. All errors of fact or interpretation are of course the responsibility of the authors.

References

[1]Porco, C.C., Helfenstein, P., Thomas, P.C., Ingersoll, A.P., Wisdom, J., West, R., Neukum, G., Denk, T., Wagner, R., Roatsch, T., Kieffer, S., Turtle, E., McEwen, A., Johnson, T.V., Rathbun, J., Veverka, J., Wilson, D., Perry, J., Spitale, J., Brahic, A., Burns, J.A., DelGenio, A.D., Dones, L., Murray, C.D., Squyres, S., "Cassini observes the active south pole of Enceladus," Science 311, 43–64 (2006).

[2]Waite, H.J., et al, "Cassini Ion and Neutral Mass Spectrometer: Enceladus Plume Composition and Structure," Science 311, 1419 (2006).

[3]Spitale, J.N., and Porco, C.C., "Association of the jets of Enceladus with the warmest regions on its south-polar fractures," Nature 449, 695–697 (2007).

[4]Smith-Konter, B., and Pappalardo, R.T., "Tidally driven stress accumulation and shear failure of Enceladus' tiger stripes," Icarus 198, 435–451 (2008).

[5]Hansen, C.C., Esposito, L., Stewart, I.F., Colwell, J., Hendrix, A., Pryor, W., Shemansky, D., and West, R., 2006, "Enceladus' Water Vapor Plume," Science 311, 1422.

[6]Chiang, R.Y., Breckenridge, W.G., and Wong, E., "Self-tuning Thruster Control for Cassini Spacecraft," Proceedings of the AIAA Guidance, Navigation, and Control Conference, San Diego, California, July 28–31, 1996.

[7]Barber, T.J. and Cowley, R.T., "Initial Cassini Propulsion System In-Flight Characterization", AIAA-2002-4152. 38th AIAA/ASME/SAE/ASEE Joint Propulsion Conference and Exhibit, Indianapolis, Indiana, July 7–10, 2002.

[8]Emily Burrough and Lee, A.Y., "Pointing Stability Performance of the Cassini Spacecraft," Journal of Spacecraft and Rockets, Volume 46, No. 5, September-October, 2009, pages 1007–1015.

[9]Lee, A.Y., and Hanover, G., "Cassini Attitude Control System Flight Performance," AIAA Guidance, Navigation, and Control Conference and Exhibit, AIAA-2005-6269, San Francisco, CA, Aug. 15–18, 2005.

[10]Macala, G.A., "Design of the Reaction Wheel Attitude Control System for the Cassini Spacecraft," Paper AAS 02-121, AAS/AIAA Space Flight Mechanics Meeting, San Antonio, Texas, January 27–30, 2002.

[11]Rappaport, N.J., Iess, L., Tortora, P., Anabtawi, A., Asmar, S., Somenzi, L., and Zingoni, F., "Mass and Interior of Enceladus from Cassin Data Analysis," Icarus, 190(2007), pp. 175–178.

[12]Feldman, A.W., Brown, J.M., Wang, E.K., Peer, S.G., and Lee, A.Y., "Reconstruction of Titan Atmosphere Density using Cassini Attitude Control Flight Data," 17th AAS/AIAA Space Flight Mechanics Meeting, AAS-07-187, Sedona, AZ, Jan. 28–Feb. 01, 2007.

[13]Sarani, S., "A Novel Methodology for Reconstruction of Titan Atmospheric Density Using Cassini Guidance, Navigation, and Control Data," Paper AIAA 2007-6343, Proceedings of the AIAA Guidance, Navigation, and Control Conference, August 20–23, Hilton Head, South Carolina, 2007.

[14]Sarani, "Enceladus Plume Density Modeling and Reconstruction for Cassini Attitude Control System," SpaceOps 2010, April 25–30, 2010, Paper 2010-2035.

[15]Lee, Allan Y., Eric K. Wang, Emily B. Pilinski, Glenn A. Macala, and Antonette Feldman, "Reconstruction of Plume Torque Imparted on the Cassini Spacecraft During an Enceladus Flyby on Reaction Wheels," Proceedings of the AIAA Guidance, Navigation, and Control Conference, August 2–5, Toronto, Ontario, Canada, 2010.

[16]Antonette Feldman and Allan Y. Lee, "Inflight Estimations of Cassini Spacecraft Inertia Tensor and Thruster Magnitude," Paper AAS 06-102, 16th AAS/AIAA Space Flight Mechanics Conference, Tampa, Florida, January 22–26, 2006. Also in Spaceflight Mechanics 2006, Volume 124, Part 1 Advances in the Astronautical Sciences.

[17]David Bates and Lee, A.Y., "In-flight Characterization of the Cassini Reaction Control Thrusters," Paper AIAA 2007-6342, Proceedings of the AIAA Guidance, Navigation, and Control Conference, August 20–23, Hilton Head, South Carolina, 2007.

[18]Boice, D.C., Soderblom, L.A., Britt, D.T., Brown, R.H., Sandel, B.R., Yelle, R.V., Buratti, B.J., Hicks, M.D., Nelson, R.M., Rayman, M.D., Oberst, J., and Thomas, N., "The Deep Space 1 Encounter with Comet 19p/Borrelly," Earth, Moon, and Planets, 89, pp. 301–324, 2002.

[19]Teolis, B.D., Perry, M.E., Magee, B.A., Westlake, J., and Waite, J.H., "Detection and measurement of ice grains and gas distribution in the Enceladus plume by Cassini's Ion Neutral Mass Spectrometer" Journal of Geophysical Research, 115, A09222, 2010.

Appendix A

Enceladus Flybys Studied in this Research

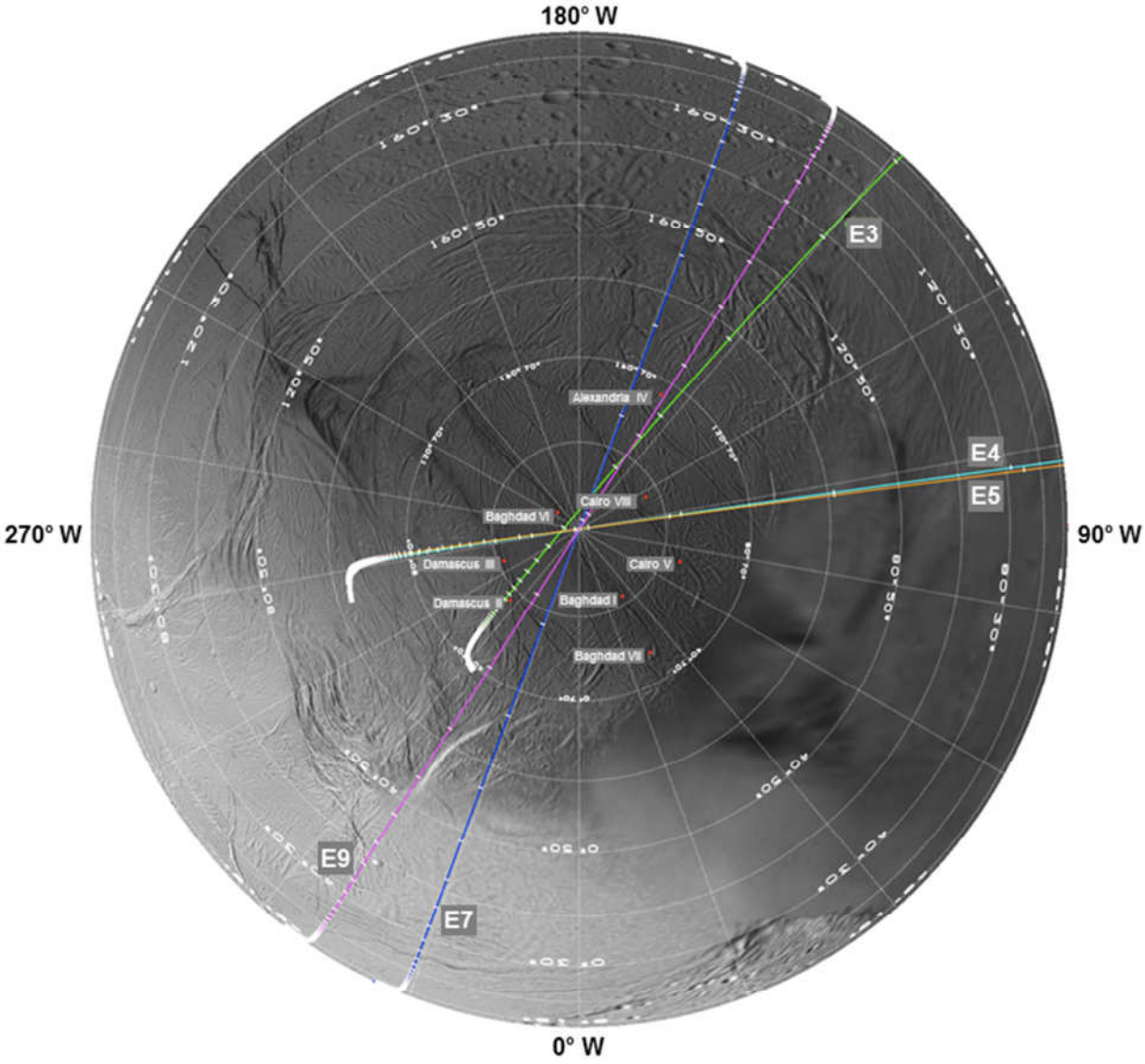

Fig. A1 Enceladus Flyby Trajectories Projected on the Equatorial Plane of Enceladus